PAPER

Modeling of high harmonic fast wave scenarios for NSTX Upgrade

IOP Publishing | International Atomic Energy Agency Nuclear Fusion

Nucl. Fusion **59** (2019) 086006 (14pp) https://doi.org/10.1088/1741-4326/ab1d7f

Modeling of high harmonic fast wave scenarios for NSTX Upgrade*

N. Bertelli[1], M. Ono[1] and E.F. Jaeger[2]

[1] Princeton Plasma Physics Laboratory, Princeton, NJ 08540 United States of America
[2] XCEL Engineering Inc., 1066 Commerce Park Drive, Oak Ridge, TN 37830, United States of America

E-mail: nbertell@pppl.gov

Received 21 December 2018, revised 1 April 2019
Accepted for publication 29 April 2019
Published 21 June 2019

Abstract

NSTX-Upgrade will operate with toroidal magnetic fields (B_T) up to 1 T, nearly twice the value used in the experiments on NSTX, and the available neutral beam injection (NBI) power will be doubled. The doubling of B_T while retaining the 30 MHz RF source frequency has moved the heating regime from the high harmonic fast wave (HHFW) regime used in NSTX to the mid harmonic fast wave regime. By making use of the full wave code AORSA (assuming a Maxwellian plasma), this work explores different HHFW scenarios for two possible antenna frequencies (30 and 60 MHz) and with and without NBI. Both frequencies have large electron absorption for large wave toroidal number particularly without NBI. With the presence of NBI, the fast ions absorption can be dominant in some scenarios. Therefore, a competition between electron and fast ion absorption is clearly apparent partially explaining why in previous NSTX HHFW experiments, a less efficient electron heating was observed. Moreover at the toroidal field of 1 T, a direct thermal ion damping might be possible under the condition when the ion temperature is larger than electron temperature. In general, the electron and ion absorption are found very sensitive to the ratio of electron and ion temperature. The impact of the hydrogen species is also studied showing that, for hydrogen concentration below 2%, the hydrogen absorption is not significant. However, a larger hydrogen concentration could open up new HHFW heating scenarios in NSTX-U. Launching at high toroidal wave number appears to be one way to significantly reduce the ion damping and in turn to obtain large electron damping in the core which can play an important role in the transport studies for NSTX-U. Finally, an higher magnetic field could also playing a role in increasing the electron temperature and consequently the electron absorption. Indeed a magnetic field scan is also shown and discussed.

Keywords: HHFW, NSTX-U, fast wave, RF heating

(Some figures may appear in colour only in the online journal)

1. Introduction

The NSTX-Upgrade (NSTX-U) project [1, 2] consists of two main elements: (i) a new and more powerful center-stack and (ii) a tangentially-aiming second neutral beam injection (NBI) system. More specifically, NSTX-U will double the toroidal magnetic field from $B_T \sim 0.5$ T to 1 T, the plasma current from $I_P \sim 1$ MA to 2 MA, and the NBI heating and current drive power up to 10 MW. One of the mission of NSTX-U is to advance the spherical tokamak (ST) concept as a possible fusion nuclear science facility (FNSF) or pilot plant [3–6]. Beyond these NSTX-U capabilities listed above, the project will retains the previous 6 MW high-harmonic fast wave (HHFW) system for heating and current drive [7, 8]. A very important question for ST-FNSF is indeed the choice of heating and current drive source. Apart from NBI and electron Bernstein waves (EBW) commonly considered for ST devices, HHFW system in NSTX demonstrated the capability

* This article is dedicated to the memory of Joel C. Hosea.

to heat the plasma electrons to temperature large than 6 keV [9]. However, the current driven by HHFW was found to be relatively low [8, 10] and HHFW has been less effective to heat H-mode plasma in the presence of NBI with respect to L-mode plasma [11, 12]. At the same time, under certain conditions, a strong interaction between HHFW and scrap-off layer has been found leading to a RF power losses. A series of works has been published on this subject [8, 13–18]. The RF edge power losses are generally expected to be reduced and more favorable to HHFW performance in the higher magnetic field of NSTX-U. In this work, we will examine the HHFW performance in order to investigate what are the best plasma conditions to take advantage of the HHFW system in NSTX-U with a larger B_T, which, in turn, can help to increase the electron temperature and consequently the electron absorption. For $B_T = 1$ T and assuming an antenna frequency $f = 30$ MHz (which corresponds to the antenna frequency used in NSTX), the first and second harmonics of hydrogen (H) are located at the high-field side and in the core plasma, respectively. As a consequence, part of the HHFW injected power can be absorbed by the H population. This new operating regime might open up new HHFW scenarios, which, in turn, can also be relevant for the initial ITER experiments with 10 MW of ICRH during the hydrogen plasma phase. Therefore, it is also of interest to investigate the impact of the H species on HHFW performance in NSTX-U plasmas.

For all the reasons mention above, the purpose of this work is to investigate a series of HHFW scenarios for NSTX-U plasma with $B_T = 1$ T by making use of the full wave code AORSA, which includes 'all-orders' kinetics effects in the dielectric tensor [19]. This aspect is very important for HHFW simulations in NSTX-U because the ion Larmor-radius effects play an significant role and therefore a complete description of the dielectric tensor is necessary. In particular, a series of AORSA simulations for two possible antenna frequencies $f = 30$ and 60 MHz are performed. The antenna frequency $f = 30$ MHz corresponds to the frequency utilized in the NSTX experimental campaign and currently set for NSTX-U. However, at $B = 1$ T the fundamental and the second hydrogen harmonics resonance are in the plasma and their roles need to be clarify. If $f = 60$ MHz were used, this frequency would reproduce scenarios already adopted in NSTX, at least in terms of deuterium and hydrogen cyclotron resonances in the plasma. We also consider the scenarios with and without neutral beam injection (NBI) and all three main components of the wave toroidal number $|n_\phi| = 5, 12$, and 21, which correspond to three different antenna phasing [8, 9].

More specifically, this paper is structured as follows: in section 2, a very brief description of the full wave code AORSA utilized for the presnet HHFW modeling is presented. Section 3 shows the NSTX-U scenarios and plasma kinetic profiles employed in the full wave simulations. The hydrogen absorption in NSTX-U plasma with $B_T = 1$ T together with a hydrogen concentration scan is presented in section 4. In section 5, electron temperature and density scans with an constant electron beta for $B_T = 1$ T NSTX-U plasma is shown. Sections 6 and 7 show a magnetic field scan with a constant electron beta and a magnetic field scan with varying the electron temperature for constant the electron density. Finally, the main conclusions of the present work are summarized in section 8.

2. The full wave code AORSA

AORSA (all-orders spectral algorithm) is a full-wave code, which solves the Helmholtz wave equation for a tokamak geometry [19]. The dielectric tensor implemented in AORSA is a complete non-local, integral operator valid for 'all orders', by taking into account all contributions in $k_\perp \rho_i$ ($k_\perp \rho_i$ are the perpendicular component of the wave vector relative to the local equilibrium magnetic field and the ion Larmor radius, respectively). Therefore, the main absorption mechanisms, such as Landau damping, transit-time magnetic pumping (TTMP), and the ion cyclotron damping are included in the code. The 'all-orders' aspect is crucial for NSTX-U HHFW in which the ion Larmor radius is often larger than the perpendicular wavelength and the ion-cyclotron harmonic number can be large. AORSA uses a Fourier decomposition in the Cartesian coordinates x and y (in the poloidal plane) and in the toroidal direction of symmetry (ϕ), $\exp(in_\phi\phi)$ (n_ϕ is the toroidal mode number). More details of the AORSA code are found in [19]. Furthermore, we employ here the latest AORSA version where a new plasma dispersion function has been implemented including a more accurate physics for the electron Landau damping and a reduce numerical pollution for strong electron Landau damping cases [20]. In this work we are focused on the core plasma so we do not employ the AORSA extension, which includes the scrape-off region beyond the last closed flux surface where the magnetic field lines are open [17, 18, 21, 22].

3. NSTX-U scenario(s) considered

The NSTX-U scenario considered is shown in figure 1. Figure 1(*a*) shows the magnetic flux surfaces whereas figures 1(*b*) and (*c*) show the plasma kinetic profiles. Magnetic equilibrium and profiles are scaled version from actual NSTX discharges [23]. In particular, figure 1(*b*) shows the electron (blue line) and ion (red line) density profiles as a function of the square root of the normalized poloidal flux, ρ_{pol}. Figure 1(*c*) shows the electron (blue line) and the ion (red line) temperature profiles as a function of ρ_{pol}. The central electron and ion temperatures are given by $T_e(0) = 1.22$ keV and $T_i(0) = 1.43$ keV, respectively. The central electron density is $n_e(0) = 5.5 \times 10^{19}$ m^{-3}. In this analysis we assume the same temperature profile for thermal ion species (deuterium, hydrogen, and carbon), while for the beam ions temperature (T_{bi}) we have adopted an effective temperature (namely, an equivalent Maxwellian) given by [24]

$$T_{bi} = \frac{2}{3}\frac{E}{n_{fast}}, \tag{1}$$

where E and n_{fast} are the total energy density profile and the density of the beams ions, respectively. Both these quantities are provided by the TRANSP simulations [23, 25, 26].

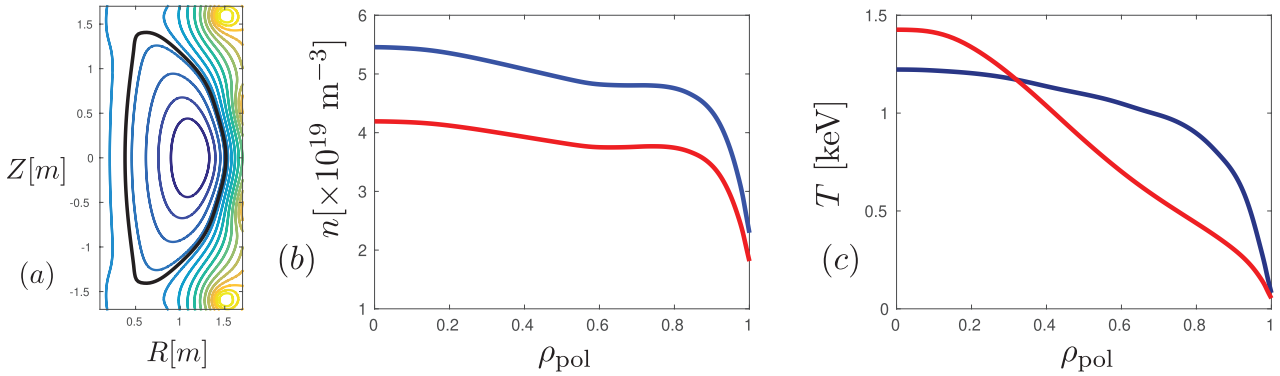

Figure 1. Magnetic equilibrium (figure (*a*)), density (figure (*b*)) and temperature (figure (*c*)) profiles of electron (blue lines) and the thermal deuterium (red lines) as a function of the square root of the normalized poloidal flux, $\rho_{\rm pol}$.

We consider two wave frequency regimes in the simulations: (i) $f = 30$ MHz, which corresponds to the frequency of the current HHFW heating system, and (ii) $f = 60$ MHz that have different deuterium and hydrogen cyclotron resonances in the plasma. For $B_{\rm T} = 1$ T and $f = 30$ MHz, the first and second harmonics of hydrogen (H) are located at the high-field side and in the core plasma, respectively (as shown in figure 3(*a*)). Moreover, at $B = 1$ T, doubling the wave frequency to 60 MHz would reproduce the scenario already adopted in NSTX (at least, in terms of deuterium and hydrogen cyclotron resonances in the plasma) as shown in figures 2(*b*) and 3(*b*). From figure 2, it is important to note the high number of deuterium cyclotron resonances present in the plasma generating a strong interaction between fast ions and HHFW, as observed experimentally [27, 28]. In order to investigate the impact of H species on the power partitioning among electron, thermal ions, and fast ions, four values (1, 2, 5, and 10%) of the H concentration are also considered in the AORSA simulations with and without NBI and for both $f = 30$ and 60 MHz (see section 4). Moreover, three values of the toroidal wave numbers are used $n_\phi = -5, -12, -21$, which correspond to three different atenna phasings. In the following sections, several parameter scans are shown and discussed: (i) the role of the hydrogen in the $B_{\rm T} = 1$ T NSTX-U plamsas and the impact of the hydrogen species concentration; (ii) a electron temperature and density scan keeping the electron beta constant; (iii) a magnetic field scan with constant electron beta; and finally (iv) magnetic field and electron temperature scan with a fixed electron density.

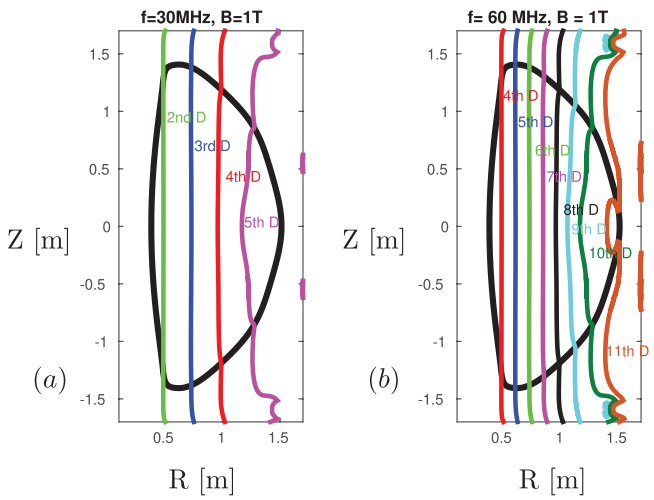

Figure 2. Deuterium (D) cyclotron resonances for an NSTX-U $B = 1$ T plasma assuming $f = 30$ MHz (figure (*a*)) and 60 MHz (figure (*b*)).

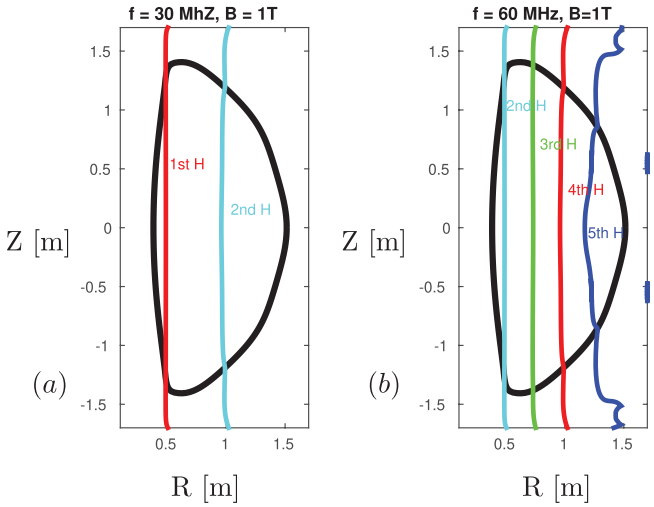

Figure 3. Hydrogen (H) cyclotron resonances for an NSTX-U $B = 1$ T plasma assuming $f = 30$ MHz (figure (*a*)) and 60 MHz (figure (*b*)).

4. Hydrogen absorption for NSTX-U $B = 1$T plasma

Operating NSTX-U at $B_{\rm T} = 1T$ retaining the 30 MHz RF source frequency has two main consequences: (i) the heating regime moves from the high harmonic fast wave (up to 11th deutrium harmonic in the confined plasmas) regime used in NSTX [8, 9] to the mid harmonic fast wave regime (up to 5th/6th D harmonic in the confined plasma), as shown in figure 2(*a*); (ii) the first and second harmonics of H are located at the high-field side and in the core plasma, respectively (as shown in figure 3(*a*)). As a consequence, part of the HHFW injected power can be absorbed

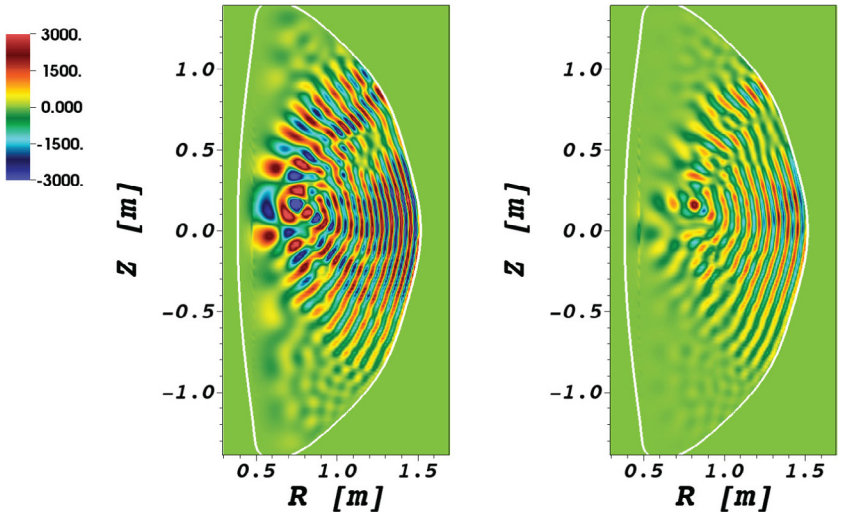

(a) (b)

Figure 4. Real part of the right-handed wave electric field, $\mathrm{Re}(E_-)$ (figure (*a*)) and left-handed wave electric field, $\mathrm{Re}(E_+)$ (figure (*b*)) for an NSTX-U plasma shown in figure 1 for $n_\phi = -12, f = 30$ MHz, and assuming 5% hydrogen concentration. The white curves represents the last closed flux surface.

by the H population. For this reason, we perform here a scan in the H concentration for different scenarios.

Figure 4 shows the wave electric field propagation evaluated by the AORSA code for the NSTX-U plasma as shown in figure 1 with antenna frequency $f = 30$ MHz. In particular, figures 4(*a*) and (*b*) show the real part of the right-handed wave electric field, $\mathrm{Re}(E_-)$ and left-handed wave electric field, $\mathrm{Re}(E_+)$ respectively, for $n_\phi = -12$ and assuming 5% H concentration. The white curve represents the last closed flux surface (LCFS). Figure 5 shows the 2D contour plot of the electron (figure 5(*a*)), hydrogen (figure 5(*b*)), and fast ions (figure 5(*c*)) power deposition corresponding to the plasma parameters used in figure 4. In these full wave simulations the injected power is fully absorbed (this is valid for all simulations presented in this work). The electron power deposition is quite broad, from the outboard (just inside the last closed flux surface) to the core plasma, whereas the H power deposition is clearly localized around the second H cyclotron resonance, which is, in this specific case, located just inboard with respect to the magnetic axis (see also figure 3(*a*)). It should be noted that the fundamental H power absorption is minimal because of the poor wave accessibility. In fact, from figure 4 one can see a weak electric field at the location of the first H cyclotron resonance (just beyond the cut-off). Unlike the power absorbed by electron, fast ions power deposition (D-NBI) is localized mainly around the fourth and fifth D cyclotron resonances. It is important to note that the absorbed power by fast ions appears stronger and broader at the fifth harmonic, which is the first resonance the wave electric field encounters during its propagation from the antenna to the core plasma. Figure 6 shows the corresponding flux surface averaged power density deposition of all plasma species (D, C, H, D-NBI, and electron) as a function of the square root of the normalized poloidal flux, ρ_{pol}. Figure 6(*a*) includes a fast ions population unlike figure 6(*b*). These figures confirm the peak H absorption localized around the second H harmonic. Moreover, one can see the both electrons and fast ions power deposition profiles are peaked on-axis. On the other hand, for this specific case, thermal D is playing a very marginal role and thermal C absorption is essentially zero (the C concentration employed in this paper is less than 2% and it does not play any role for basically all scenarios analyzed). Comparing figures 6(*a*) and (*b*), a significant reduction of the H absorption is observed due to the presence of a fast ions population, which absorbs a large amount of power. It is important to remind the reader again that the AORSA simulations performed in this paper are not considering non-Maxwellian ion effects, which can play an important role and, in principle, affect the hydrogen and fast ion absorption. This is outside the scope of this paper but it will be investigated in a future work.

In order to further understand the observations discussed above, we performed a hydrogen concentration scan (1, 2, 5, and 10%) for the NSTX-U plasma shown in figure 1. This scan is carried out for three toroidal wave numbers ($n_\phi = -5, -12$, and -21), which represent the dominant n_ϕ components of the HHFW antenna for three different antenna phasings and two antenna frequencies, $f = 30$ and 60 MHz. We also consider NSTX-U plasma scenarios with and without NBI. Figures 7 and 8 show the absorption (in percentage) of electrons, thermal deuterium (D), and beam ions (Dbeam) as a function of the H concentration for $f = 30$ and $f = 60$ MHz, respectively. In particular, the first (second) columns of both figures 7 and 8 shows the plasma scenarios with (without) NBI. Moreover, first, second, and third row shows the results for $n_\phi = -5, -12$, and -21, respectively. The cyan, red, green, magenta, and black curves represent the electron, thermal D, thermal H, thermal C, adn NBI absorption, respectively. This color coding will be maintained for the rest of the manuscript. From these results we can make the following observations: (i) the H absorption is increasing with the H concentration, as expected; (ii) the H absorption can play a significant role for lower n_ϕ in the presence of NBI, particularly for $f = 30$ MHz; (iii) without NBI, H absorption can be up to 60% for $n_\phi = -5$ and 10% H concentration for $f = 30$ MHz; (iv) for $f = 60$ MHz, the H role is quite marginal due to the stronger electron damping and the presence of higher H cyclotron resonances

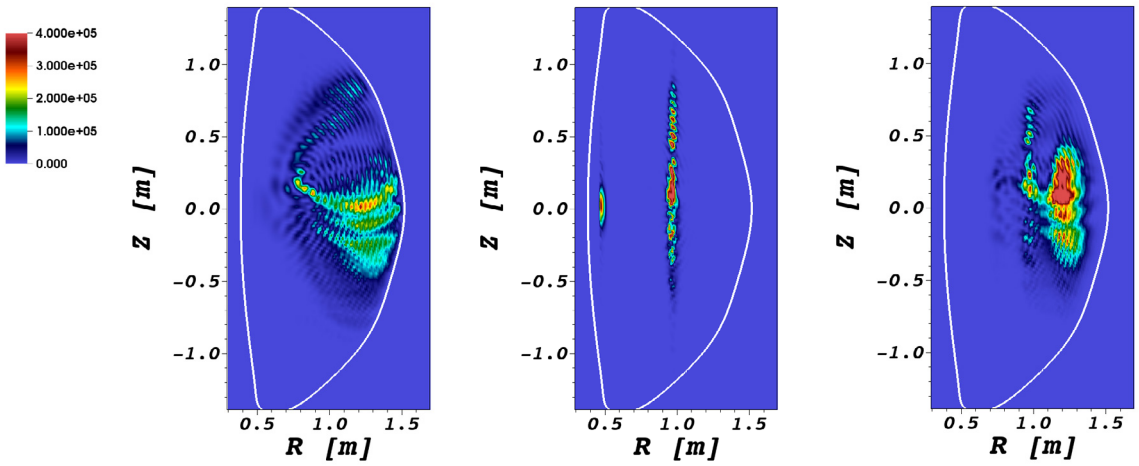

Figure 5. 2D contour plot of the electron (*a*), hydrogen (*b*), and fast ions (*c*) power deposition correspoinding to the case shown in figure 4.

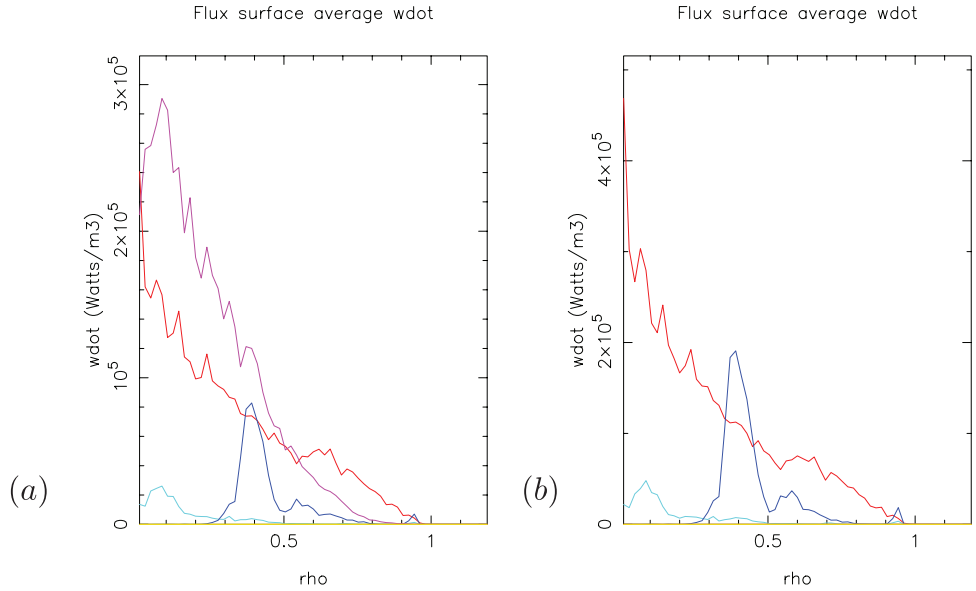

Figure 6. Flux surface averaged power density of electrons (red), thermal D (cyan), thermal H (blue), thermal carbon (yellow), and fast ions (magenta) as a function of the square root of the normalized poloidal flux, for $n_\phi = -12$ and H concentration of 5%. Figures (*a*) and (*b*) show the results with and without fast ions, respectively.

in the plasmas (both with and without NBI) as in NSTX. Overall, the electron absorption increases with n_ϕ and it tends to be dominant particularly without NBI. This aspect is even more evident for $f = 60$ MHz. The role of fast ions can be quite significant for lower $n_\phi (|n_\phi| \leqslant 12)$ for both wave frequencies. It is interesting to note that the fast ions absorption is larger for $f = 60$ MHz than $f = 30$ MHz although in the latter case we have lower D harmonic number in the plasma (where one might expect higher absorption). This is attributed to the fact that, overall, for $f = 60$ MHz, the wave electric field encounters a larger number of D cyclotron harmonic resonances with respect to the $f = 30$ MHz case (see figure 2), which makes the fast ions actually interact stronger with the wave field. From the left columns of both figures 7 and 8, one can see minor changes in the power partitioning with respect to the H concentration for all the electron and ion species. Even the thermal D absorption can be quite significant for low n_ϕ and $f = 30$ MHz without NBI. However, overall, for 2% H concentration, which is a reasonable amount representing the H population in previous NSTX experiments, the impact of the H species can be then important particularly for $f = 30$ MHz, lower n_ϕ and without NBI. It is important to mention that in the previous HHFW experiments preformed in NSTX the most common antenna phase adopted was $|n_\phi| = 12$ and 21 [8, 9]. However, the presence of the second H resonance in the plasma might results in possible new HHFW NSTX-U scenarios for the future campaign. For instance, it suggests the possibility to perform HHFW experiments in NSTX-U with H gas puff. In DIII-D, where the fast waves plasma scenarios was quite similar to the case analyzed here, they indeed observed a role of the hydrogen species with respect to the fast ion absorption (see, for instance, [29, 30]) In fact, the H power absorption localized to the second harmonic might modify the ion temperature locally and the location can change accordingly to the magnetic field value. On the other hand, due to the high-energy (non-Maxwellian) tail of the

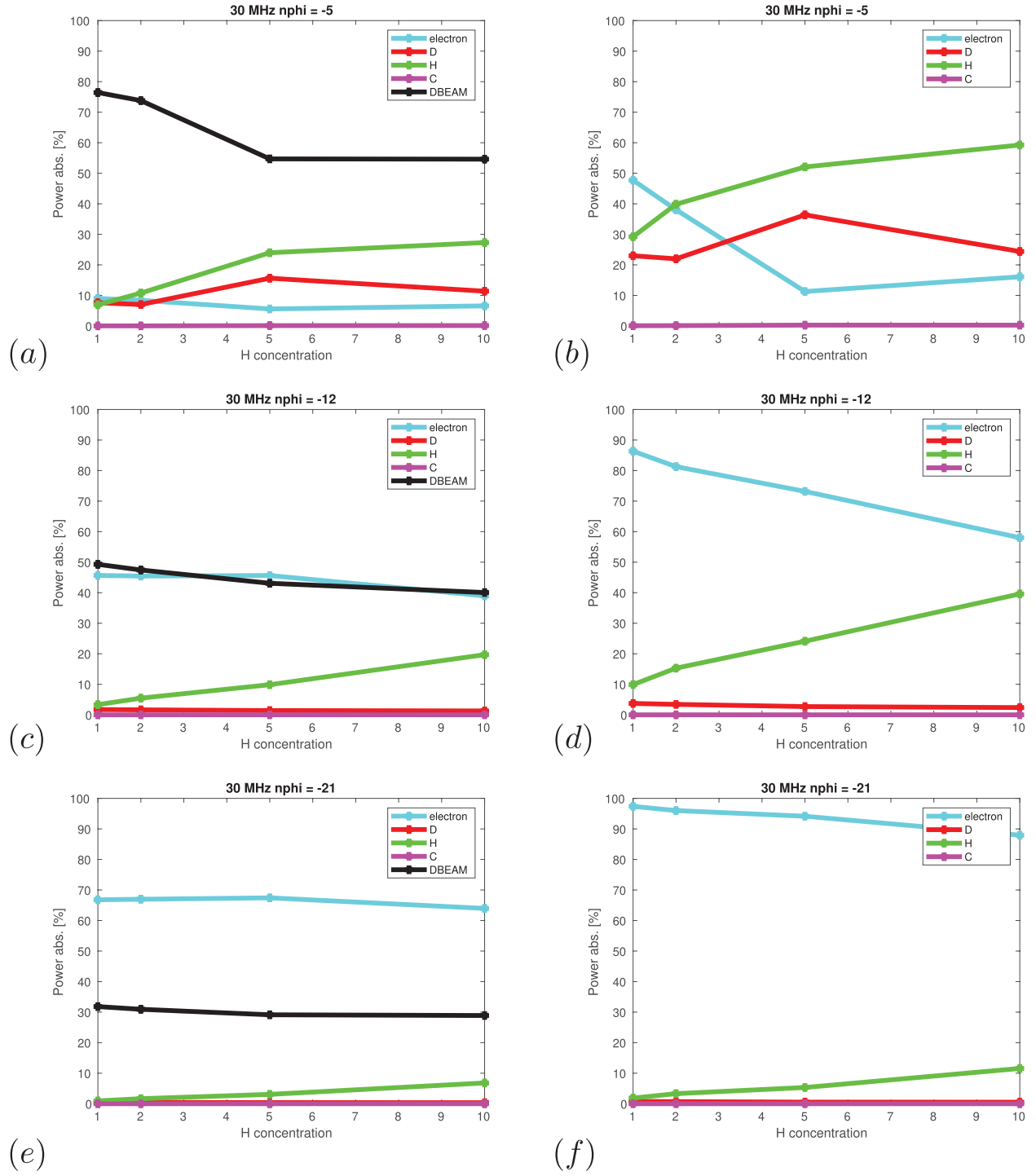

Figure 7. Absorption of electrons, thermal deuterium (D), thermal hydrogen (H), thermal carbon (C), and fast ions (Dbeam) as a function of the H concentration (1, 2, 5, and 10%) for NSTX-U plasma assuming $f = 30$ MHz. First column includes a fast ions population whereas second column fast ions are not present. Moreover, first, second, and third row shows the results for $n_\phi = -5, -12$, and -21, respectively. Black curves represent fast ion absorption, green curves represent H absorption, red curves represent thermal D absorption, and magenta curves represent C absorption (which is basically negligible).

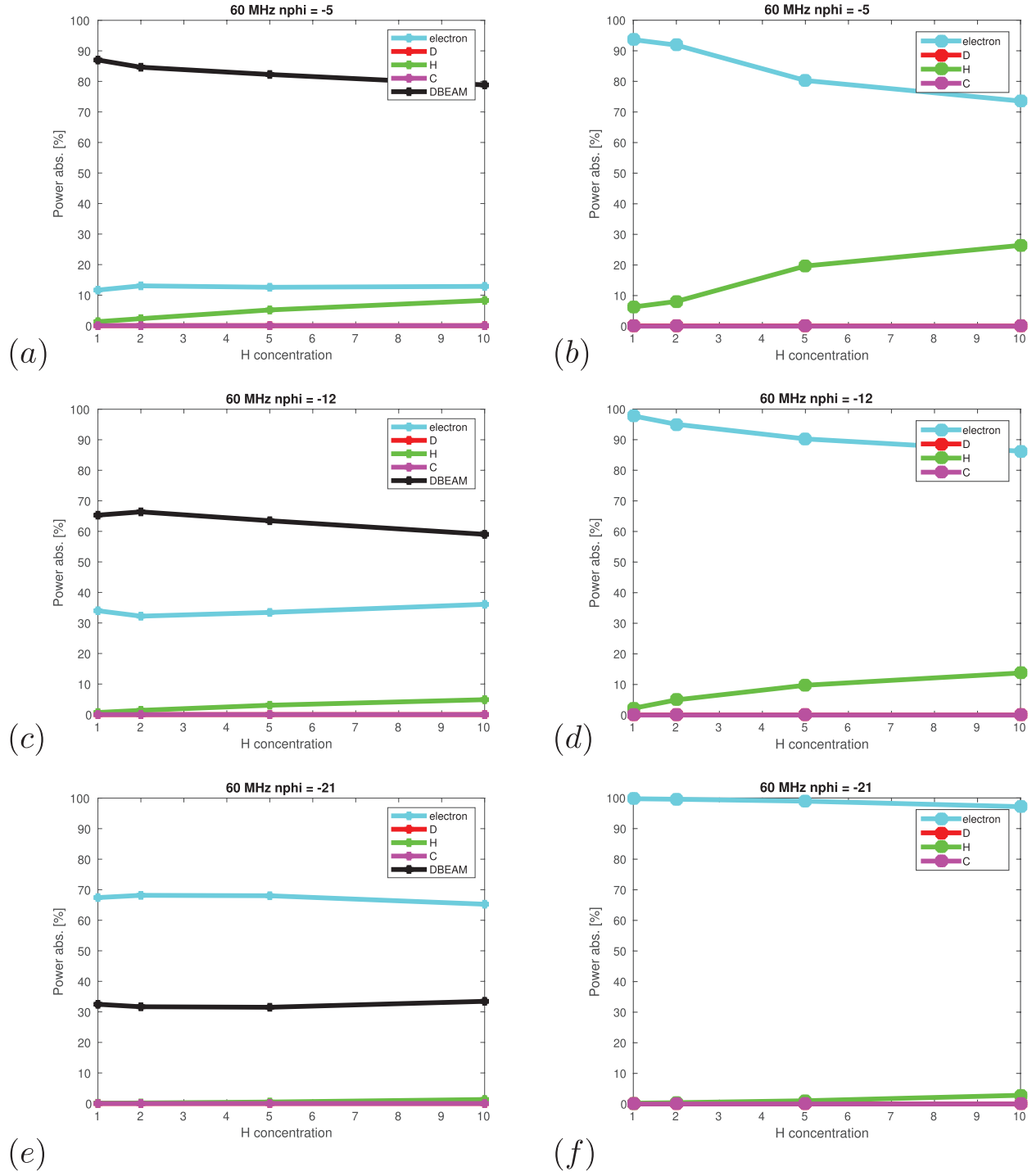

Figure 8. Absorption of electrons, thermal deuterium (D), thermal hydrogen (H), thermal carbon (C), and fast ions (Dbeam) as a function of the H concentration (1, 2, 5, and 10%) for NSTX-U plasma assuming $f = 60$ MHz. First column includes a fast ions population whereas second column fast ions are not present. Moreover, first, second, and third row shows the results for $n_\phi = -5, -12$, and -21, respectively. Black curves represent fast ion absorption, green curves represent H absorption, red curves represent thermal D absorption, and magenta curves represent C absorption (which is basically negligible).

H distribution function (caused by the acceleration of H species by HHFW), part of the H absorbed power could be transferred to electron heating via collisions, providing additional core electron heating (beyond the direct electron Landau damping) to the 'standard' HHFW performance. These aspects are not analysed here and they are not part of the scope of this work but it will be a subject of a future work to understand their feasibily.

5. Electron temperature and density scans with constant electron beta β_e

In this section we present a scan of the electron temperature and density keeping the electron beta constant (the electron beta is the ratio of the plasma pression to the magnetic pression, $\beta_e = 8\pi n_e k_B T_e / B^2$), assuming $B_T = 1$ T as used in the

previous section 4. Figures 9 and 10 show the absorption (in percentage) of electrons, thermal deuterium (D), thermal hydrogen (H), thermal carbon (C), and fast ions (Dbeam) as a function of the toroidal mode number $|n_\phi|(=5,12,21)$ assuming 2% H concentration for NSTX-U plasma shown in figure 1 with $f=30$ MHz and $f=60$ MHz, respectively. Left column of both figures includes the fast ion population whereas for second column the fast ion population is not present. The curve color coding is the same as employed in section 4, namely, in figures 7 and 8. More importantly, in these simulations the electron beta is kept constant. In particular, figures 9(*a*) and (*b*) (figures 10(*a*) and (*b*)) show the electron and ion absorption lowering T_e by 50% ($T_e(0)=0.61$ keV) and increasing n_e by 50% ($n_e(0)=11\times10^{19}$ m^{-3}) relative to the profiles shown in figure 1; figures 9(*c*) and (*d*) (figures 10(*c*) and (*d*)) uses T_e and n_e as shown in figure 1 ($T_e(0)=1.22$ keV and $n_e(0)=5.5\times10^{19}$ m^{-3}); figures 9(*e*) and (*f*) (figures 10(*e*) and (*f*)): T_e is doubled ($T_e(0)=2.44$ keV) and n_e is lowered by 50% ($n_e(0)=2.25\times10^{19}$ m^{-3}) relative to the profiles shown in figure 1; figures 9(*g*) and (*h*) (figures 10(*g*) and (*h*)): T_e is tripled ($T_e(0)=3.66$ keV) and n_e is lowered by a factor three ($n_e(0)=1.83\times10^{19}$ m^{-3}) relative to the profiles shown in figure 1. From figures 9 and 10, one can clearly note that, when n_ϕ increases, the electron absorption increases while the ion absorption decreases, in agreement with previous works on HHFW (see, for instance, [31, 32]). Higher wave toroidal number increases indeed the electron Landau damping due to a slower wave phase velocity. The lower antenna phasing corresponding to $|n_\phi|=5$ seems to be the more unfavorable for heating electrons, compared to $|n_\phi|=12$ and 21 in agreement with the NSTX experimental observations [8, 33]. This trend is an important element for the future NSTX-U experimental campaign.

Stronger absorption by thermal deuterium is found predominantly at lower n_ϕ for $f=30$ MHz. In fact, the absorption by thermal D appears sensitive to T_e/T_i, as previously observed in [24]. This aspect is even more evident for $f=30$ MHz without NBI (right column) where the thermal D absorption can be up to 50% for $n_\phi=5$. By comparison, for $f=60$ MHz, the thermal D absorption is basically negligible because of the predominant absorption by electrons and fast ions. As expected, the electron absorption tends to increase with the electron temperature and this effect is more evident in the case without NBI and stronger for $f=60$ MHz with respect to $f=30$ MHz for low n_ϕ. In the presence of NBI, the fast ion absorption is slightly larger for $f=60$ MHz than for $f=30$ MHz. This is explained by the presence of a large number of harmonic number in the confined plasma (see figure 2) although $f=30$ MHz the harmonic number is lower. For large n_ϕ the results are quite similar between the two antenna frequencies. HHFW system has experimentally demonstrated the capability to heat L-mode plasmas to very high temperatures particularly when an internal transport barrier forms [11, 12]. However, it has also been less effective to heat deuterium H-mode plasmas in the presence of NBI. This behavior can been partially understood by both figures 9 and 10, where a large fast ion absorption is always present when NBI are included in the simulation. On the other hand, a dominant electron damping is evident in the case without NBI consistent with the previous experimental observations. However, it is important to mention that another aspect that can reduce the efficiency of the HHFW system is the role of RF srape-off layer losses as shown in experimental [8, 13–16] and modeling [17, 18, 34] works. These numerical results, however, suggest that a combination of HHFW and NBI can be possible by adopting higher n_ϕ, which corresponds to the proper antenna phasing for electron heating, and modifying the NBI input power accordingly. The future NSTX-U experimental campaign with the new more tangential NBI beam should be able to validate the numerical results presented here. Regarding the H absorption, as discussed in the previous section, it can be significant mainly for low n_ϕ but it is also sensitive, as found for the thermal D, to the ratio T_e/T_i and n_e. See, for example, figure 10(*b*) with lower temperature and higher density, the H absorption can be up to 50%. Moreover, it is interesting to note that, for $f=30$ MHz, at lower electron temperature and higher density (figures 9(*a*) and (*b*)) the thermal D absorption is larger than the H absorption but then the behavior is opposite. This is due to the large absorption at the fifth D cyclotron resonance, which is the first resonance encountered by the wave electric field. Therefore, for both lower electron temperature (consequently, higher ion temperature) and higher electron density (consequently, higher ion density) the thermal D has a dominant role with respect to the thermal H. For $f=60$ MHz, one cannot see the same behavior because of the higher harmonic number for both thermal D and H species.

6. Magnetic field scan with constant electron beta β_e

One of the main new capability of NSTX-U will be to operate at toroidal magnetic field at magnetic axis up to $B_T=1$ T, unlike NSTX in which the higher magnetic field range was about $B_T=0.5$ T. In fact, during the initial NSTX-U research operations in 2016, NSTX-U was already operating at higher field compared to NSTX, namely, $B_T=0.63$ T [2, 35, 36]. For this reason, a toroidal magnetic field scan is performed in order to cover different NSTX-U scenarios. In particular, we employ the same magnetic configuration and plasma profiles as shown in figure 1, just rescaling the magnetic field values to four different values: $B=0.53, 0.63, 0.76$, and 1.0 T to cover NSTX and possible future NSTX-U scenarios. The reason to maintain the same magnetic geometry was done in order to minimize the differences between different scenarios and, at the same time, emphasize only the change in the magnetic field values. Regarding the kinetic profiles, they change accordingly to the magnetic field in order to keep the electron beta constant. Figure 11 shows the absorption (in percentage) of electrons, thermal deuterium (D), thermal hydrogen (H), thermal carbon (C), and fast ions (Dbeam) as a function of the toroidal mode number $|n_\phi|(=5,12,21)$ assuming 2% H concentration for NSTX-U plasma shown in figure 1 with $f=30$ MHz. Left column of both figures includes a fast ions population whereas second column fast ions population are not present.

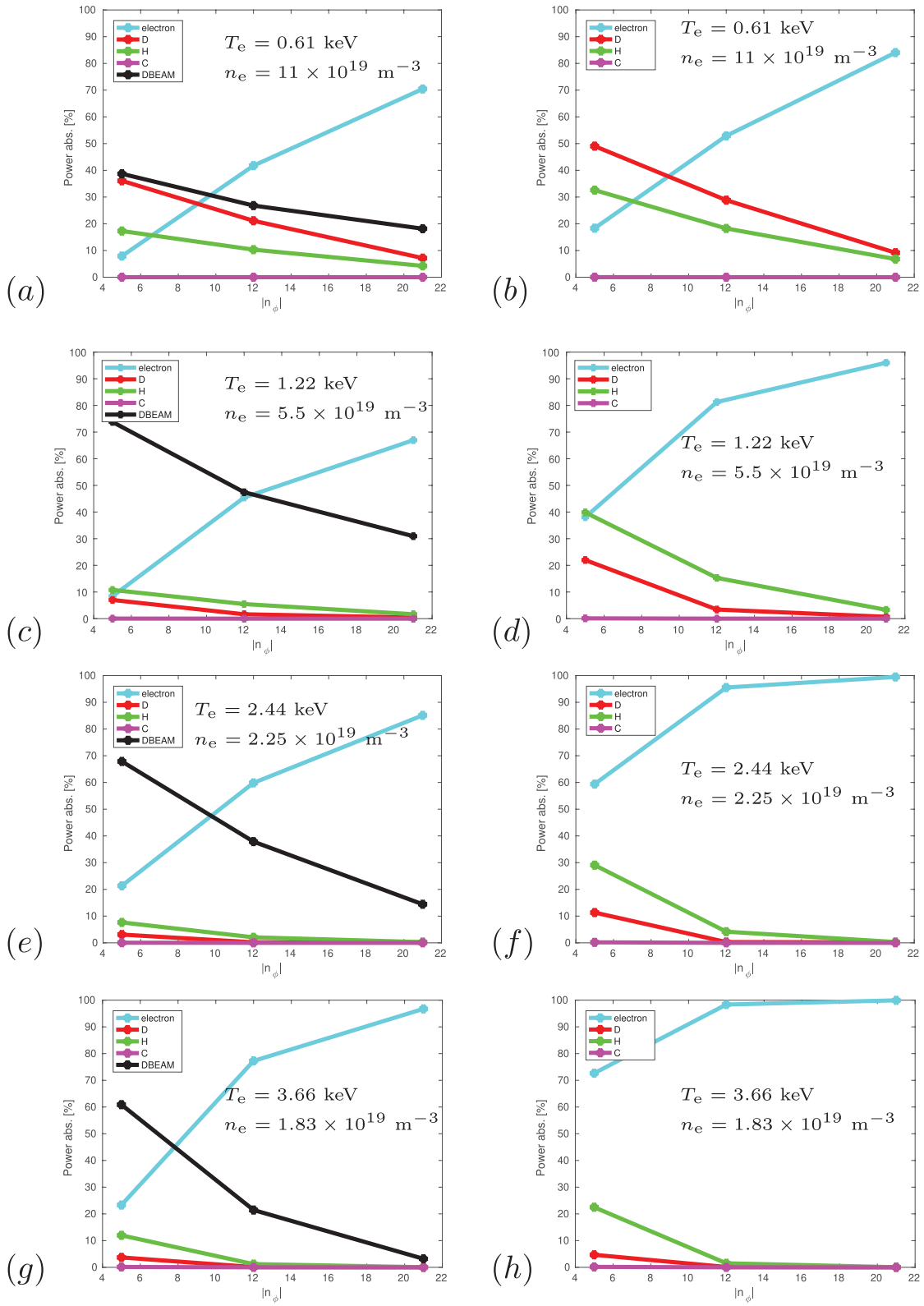

Figure 9. Absorption of electrons, thermal deuterium (D), thermal hydrogen (H), thermal carbon (C), and fast ions (Dbeam) as a function of the toroidal mode number $|n_\phi|$ assuming 2% H concentration for NSTX-U plasma shown in figure 1 with $f = 30$ MHz and constant electon beta. The left column ((*a*), (*c*), (*e*), and (*g*)) includes a fast ions population whereas the right column ((*b*), (*d*), (*f*), and (*h*)) fast ions are not present. Black curves represent fast ion absorption, green curves represent H absorption, red curves represent thermal D absorption, and magenta curves represent C absorption. The temperature and the density values are shown in each panel.

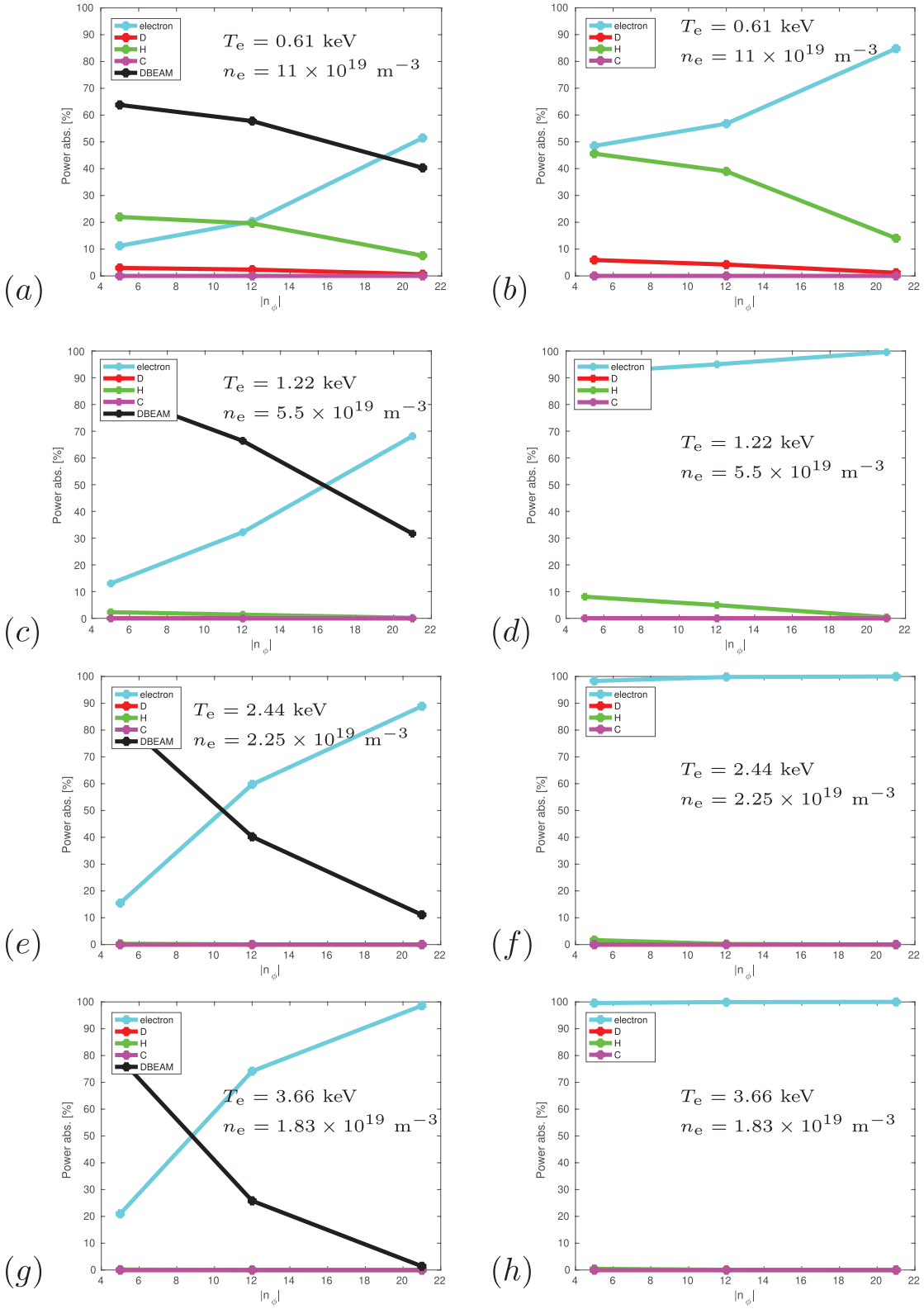

Figure 10. Same as figure 9 with $f = 60$ MHz. The temperature and the density values are shown in each panel.

The curve color coding is the same as employed in previous sections. As done in section 5, in this simulations the electron beta is kept constant so we are using the same profile shown in figure 1 but rescaled accordingly. More specifically, in figures 11(*a*) and (*b*) the magnetic field is $B_T(0) = 0.53$ T and the electron temperature and density are the same as shown in figure 1 ($T_e(0) = 1.22$ keV and $n_e(0) = 5.5 \times 10^{19}$ m^{-3}); in figures 11(*c*) and (*d*) the magnetic field is $B_T(0) = 0.63$ T

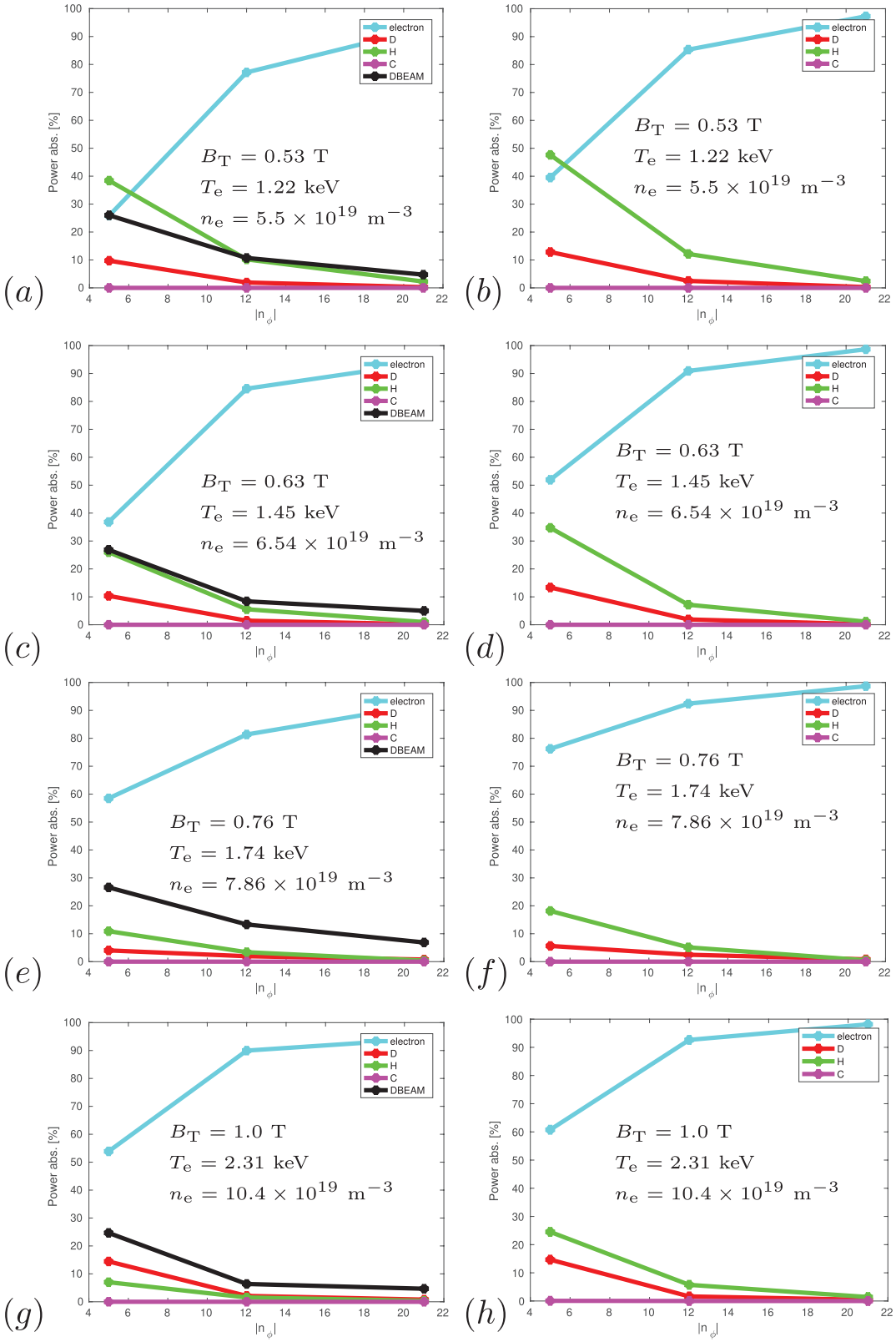

Figure 11. Absorption of electrons, thermal deuterium (D), thermal hydrogen (H), thermal carbon (C), and fast ions (Dbeam) as a function of the toroidal mode number n_ϕ assuming 2% H concentration for NSTX-U plasma shown in figure 1 with $f = 30$ MHz and constant electon beta. The left column ((*a*), (*c*), (*e*), and (*g*)) includes a fast ions population whereas the right column ((*b*), (*d*), (*f*), and (*h*)) fast ions are not present. Color coding the same as used in the previous figures and shown in the figures. The magnetic field, temperature and the density values are shown in each panel.

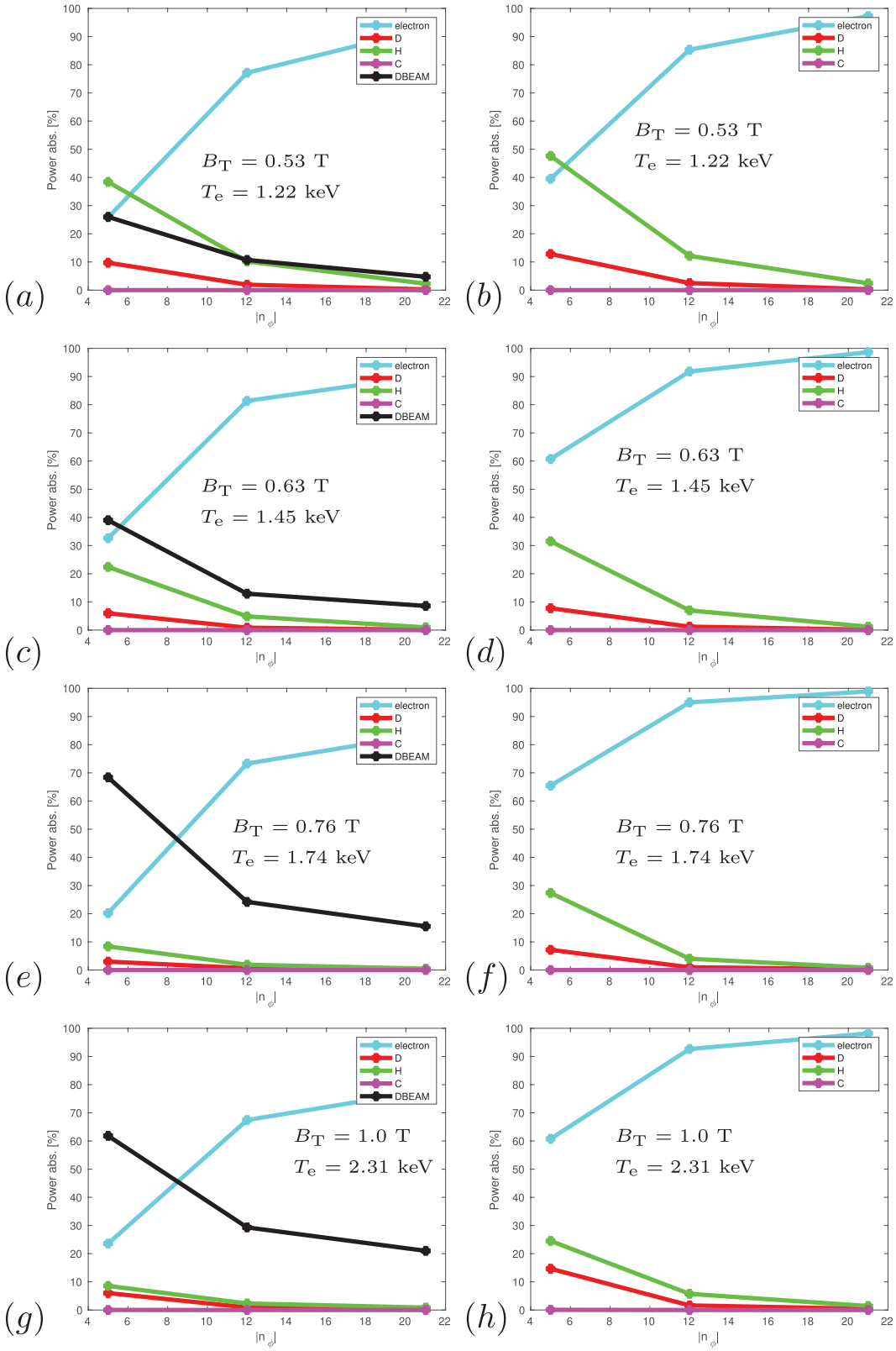

Figure 12. Absorption of electrons, thermal deuterium (D), thermal hydrogen (H), thermal carbon (C), and fast ions (Dbeam) as a function of the toroidal mode number n_ϕ assuming 2% H concentration for NSTX-U plasma shown in figure 1 with $f = 30$ MHz. The left column ((*a*), (*c*), (*e*), and (*g*)) includes a fast ions population whereas the right column ((*b*), (*d*), (*f*), and (*h*)) fast ions are not present. Color coding the same as used in the previous figures and shown in the figures. Elctron density corresponds to the density shown in figure 1 ($n_e(0) = 5.5 \times 10^{19}$ m^{-3}). The magnetic field and temperature values are shown in each panel.

and T_e and n_e are increased by the factor 1.19 ($T_e(0) = 1.45$ keV and $n_e(0) = 6.54 \times 10^{19}$ m^{-3}), which corresponds to the ratio of the two magnetic field values, $B_T(0) = 0.63$ T and $B_T(0) = 0.53$ T; in figures 11(*e*) and (*f*) the magnetic field is $B_T(0) = 0.76$ T and T_e and n_e are increased by the factor 1.43 ($T_e(0) = 1.74$ keV and $n_e(0) = 7.86 \times 10^{19}$ m^{-3}), which corresponds to the ratio of the two magnetic field values, $B_T(0) = 0.76$ T and $B_T(0) = 0.53$ T; figures 11(*g*) and (*h*) the magnetic field is $B_T(0) = 1.0$ T and T_e and n_e are increased by the factor 1.89 ($T_e(0) = 2.31$ keV and $n_e(0) = 10.4 \times 10^{19}$ m^{-3}), which corresponds to the ratio of the two magnetic field values, $B_T(0) = 1.0$ T and $B_T(0) = 0.53$ T. From figure 11, one can see that the electron absorption tends to slightly increase with higher magnetic field. This behavior is more evident for lower n_ϕ. For $n_\phi = -21$, the electron damping is so dominant that the ion/fast ion species do not play any role. The electron absorption is always above 90%. On the other side, the fast ion absorption is almost constant in these cases and below 30%. H absorption tends to decrease with higher B_T, with and without NBI, except for $B_T = 1$ T without NBI where the second H resonance is located in core plasma. The thermal D absorption is basically negligible for $|n_\phi| > 12$ with and without NBI for all magnetic field values. The main contribution is up to about 15%. The analogous simulations for $f = 60$ MHz have been also performed but we do not show them here mainly because they do not indicate any particular behaviors with the respect to the $f = 30$ MHz. The only main difference is that for $f = 60$ MHz we have a dominant electron absorption even with lower $|n_\phi|$.

7. Magnetic field and electron temperature scan

Finally, we present here both magnetic field and electron temperature scan keeping the electron density equal to the case shown in figure 1. This scan tries to simulate the effect of increased electron temperature (or electron energy confinement) with toroidal magnetic field as observed in many tokamak experiments. Figure 12 shows the absorption (in percentage) of electrons, thermal deuterium (D), thermal hydrogen (H), thermal carbon (C), and fast ions (Dbeam) as a function of the toroidal mode number $|n_\phi|(= 5, 12, 21)$ assuming 2% H concentration for NSTX-U magnetic configuration shown in figure 1 with only $f = 30$ MHz. Left column of both figures includes a fast ions population whereas second column fast ions population are not present. The curve color coding is the same as employed in the previous sections. In particular, in figure 12 the density is fixed to the case shown in figure 1. Moreover, in figures 12(*a*) and (*b*) the magnetic field is $B_T(0) = 0.53$ T and the electron temperature is the same as shown in figure 1 ($T_e(0) = 1.22$ keV. Therefore, figures 12(*a*) and (*b*) are the same as figures 11(*a*) and (*b*). In figures 12(*c*) and (*d*) the magnetic field is $B_T(0) = 0.63$ T and T_e is increased by the factor 1.19 ($T_e(0) = 1.45$ keV); in figures 12(*e*) and 12(*f*) the magnetic field is $B_T(0) = 0.76$ T and T_e is increased by the factor 1.43 ($T_e(0) = 1.74$ keV); in figures 12(*g*) and (*h*) the magnetic field is $B_T(0) = 1.0$ T and T_e is increased by the factor 1.89 ($T_e(0) = 2.31$ keV. From these figures a competition between electron, thermal H, and fast ion damping appears (as shown in previous sections). Increasing the electron temperature should help getting higher electron absorption, however, increasing, at the same time, the magnetic field reduces the deuterium and hydrogen cyclotron harmonic number with the consequence of increasing the fast ion absorption. Looking at the left column of figure 12, one can note that the increasing of the magnetic field has a stronger effect with respect to the increasing of the electron temperature. In fact, one can see an increase of the fast ion absorption from figures (*a*)–(*g*) (left column) whereas the electron absorption does not significantly change. Thermal H absorption decreases with higher electron temperature. Without NBI, as observed in the previous sections, for large n_ϕ the electron absorption is dominant. Only at low n_ϕ the thermal H absorption play a role. Almost negligible absorption of thermal D is also seen.

8. Conclusions

Officially NSTX-U began its research operations in 2016, but a failure of a magnetic control coil resulted in the suspension of operations and initiation of recovery activities [36]. During this first NSTX-U operation, which lasted ten weeks, no HHFW was employed in the experiments. HHFW planned to be used in the next NSTX-U experimental campaign to inject external power (nominally up to 6 MW) with or without NBI (up to 10 MW). For this reason, it is important to investigate the HHFW performance under specific plasma scenarios for higher toroidal magnetic field (up to 1 T) expected in NSTX-U.

In this work, we presented a large number of 2D full wave simulations by adopting one of the most advanced ICRH full wave solver in our community named AORSA. In particular, we investigate the impact of the HHFW power on the different species in the plasma for two antenna frequencies ($f = 30$ and 60 MHz) and for $|n_\phi| = 5, 12$, and 21, which represents the three antenna phasings used with the HHFW antenna in NSTX. Assuming a magnetic field of 1 T, which is the target magnetic field value expected to be reached in NSTX-U, the first and second harmonic of the hydrogen species are within the confined plasma. The second harmonic is actually in the core plasma unlike the first harmonic, which is in the high field side region and consequently it plays a marginal role due to the poor wave accessibility. The presence of the second hydrogen harmonic can indeed modify the power partitioning we found in NSTX. Here we presented a complete hydrogen concentration scan considering four concentration values: 1%, 2%, 5%, and 10%. We found that the hydrogen absorption can be quite significant mainly without the presence of NBI and for $f = 30$ MHz. However, for a 2% concentration, which is the concentration expected in previous NSTX experiments, the hydrogen does not play a major role (both for $f = 30$ and 60 MHz and with and without NBI). nevertheless, this could, in principle, open up the opportunity of new HHFW scenarios in NSTX-U experimental campaign with active hydrogen gas puff. From the modeling point of view, an extension of this work including non-Maxwellian hydrogen effects in important

to be able to better quantify the hydrogen absorption and consequently the additional electron absorption.

Another series of simulations shows the power partitioning of the plasma species varying the electron temperature and density keeping the electron beta constant. From these simulations we observed: (i) launching at high toroidal wave number appears to be one way to significantly reduce the ion/fast on damping and in turn to obtain large electron damping; (ii) a competition between electron and fast ion absorption is clearly apparent; (iii) a direct thermal ion absorption is found particularly for lower n_ϕ and T_e. In fact, the thermal ion absorption is found to be very sensitive to the ratio T_e/T_i.

A magnetic field scan is also discussed again keeping constant the electron beta. From this scan we can summarize that a slightly increase of the electron damping is observed for higher magnetic field. This increase is more evident for low n_ϕ unlike larger n_ϕ where the electron damping is already dominant. This is quite attractive for HHFW experiments in NSTX-U because an effective lower n_ϕ is more favorable for driving current. Moreover, the increase of the magnetic field together with the increase of electron temperature can lead to an even more robust electron core heating by HHFW in NSTX-U, which could be very useful for transport studies.

Finally, the numerical results presented and discussed here suggest that a combination of HHFW and NBI can be possible in NSTX-U by adopting higher n_ϕ and modifying the NBI input power accordingly. Such experiments will be hopefully performed in the future NSTX-U experimental compaign with also the new more tangential NBI beam. Obviously, these experiments will be crucial in order to validate the numerical results presented here.

Acknowledgments

This work was supported by a U.S. Department of Energy (DOE) Scientific Discovery through Advanced Computing Initiative Contract Number DE-SC0018090 and the U.S. DOE under DE-AC02-CH0911466. The digital data for this paper can be found following the links from https://dataspace.princeton.edu/jspui/handle/88435/dsp011v53k0334. The publisher, by accepting the article for publication acknowledges, that the United States Government retains a non-exclusive, paid-up, irrevocable, world-wide license to publish or reproduce the published form of this manuscript, or allow others to do so, for United States Government purposes.

References

[1] Menard J.E. *et al* 2012 *Nucl. Fusion* **52** 083015
[2] Menard J.E. *et al* 2017 *Nucl. Fusion* **57** 102006
[3] Peng Y.K. *et al* 2005 *Plasma Phys. Control. Fusion* **47** B263
[4] Peng Y.K. *et al* 2009 *Fusion Sci. Technol.* **56** 957
[5] Menard J.E. *et al* 2011 *Nucl. Fusion* **51** 103014
[6] Menard J.E. *et al* 2016 *Nucl. Fusion* **56** 106023
[7] Ono M. 1995 *Phys. Plasmas* **2** 4075
[8] Hosea J.C. *et al* 2008 *Phys. Plasmas* **15** 056104
[9] Taylor G. *et al* 2010 *Phys. Plasmas* **17** 056114
[10] Phillips C.K. *et al* 2009 *Nucl. Fusion* **49** 075015
[11] Mazzucato E. *et al* 2008 *Phys. Rev. Lett.* **101** 075001
[12] Yuh H. *et al* 2011 *Phys. Rev. Lett.* **106** 055003
[13] Perkins R.J. *et al* 2012 *Phys. Rev. Lett.* **109** 045001
[14] Perkins R.J. *et al* 2013 *Nucl. Fusion* **53** 083025
[15] Perkins R.J. *et al* 2015 *Phys. Plasmas* **22** 042506
[16] Perkins R.J. *et al* 2017 *Nucl. Mater. Energy* **12** 283
[17] Bertelli N. *et al* 2014 *Nucl. Fusion* **54** 083004
[18] Bertelli N. *et al* 2016 *Nucl. Fusion* **56** 016019
[19] Jaeger E.F. *et al* 2001 *Phys. Plasmas* **8** 1573
[20] Berry L.A. *et al* 2016 *Phys. Plasmas* **23** 102504
[21] Green D.L. *et al* 2011 *Phys. Rev. Lett.* **107** 145001
[22] Lau C. *et al* 2018 *Nucl. Fusion* **58** 066004
[23] Gerhardt S.P., Andre R. and Menard J.E. 2012 *Nucl. Fusion* **52** 083020
[24] Bertelli N. *et al* 2014 *AIP Conf. Proc.* **1580** 310
[25] TRANSP (computer software) https://doi.org/10.11578/dc.20180627.4
[26] Hawryluk R.J. 1980 *Physics Close to Thermonuclear Conditions* vol 1 ed B. Coppi *et al* (Brussels: Commission of the European Communities) p 19
[27] Wilson J.R. *et al* 2003 *Phys. Plasmas* **10** 1733
[28] Liu D. *et al* 2010 *Plasma Phys. Control. Fusion* **52** 025006
[29] Heidbrink W.W. *et al* 1999 *Nucl. Fusion* **39** 1369
[30] Petty C.C. *et al* 2001 *Plasma Phys. Control. Fusion* **43** 1747
[31] Lashmore-Davies C.N., Fuchs V. and Cairns R.A. 1998 *Phys. Plasmas* **5** 2284
[32] Menard J. *et al* 1999 *Phys. Plasmas* **6** 2002
[33] Hosea J.C. *et al* 2009 *AIP Conf. Proc.* **1187** 105
[34] Perkins R.J. *et al* 2017 *Nucl. Fusion* **57** 116062
[35] Battaglia D.J. *et al* 2018 *Nucl. Fusion* **58** 046010
[36] Kaye S.M. *et al* 2018 *Nucl. Fusion* **59** 112007